Appl. Math. Mech. -Engl. Ed., **46**(4), 601–616 (2025)

APPLIED MATHEMATICS AND MECHANICS (ENGLISH EDITION)

https://doi.org/10.1007/s10483-025-3239-6

An origami-inspired nonlinear energy sink: design, modeling, and analysis*

Youcheng ZENG[1,2], Hu DING[1,3,4,†], J. C. JI[2]

1. Shanghai Key Laboratory of Mechanics in Energy Engineering, Shanghai Institute of Applied Mathematics and Mechanics, School of Mechanics and Engineering Science, Shanghai University, Shanghai 200444, China;
2. School of Mechanical and Mechatronic Engineering, University of Technology Sydney, NSW 2007, Australia;
3. Shaoxing Institute of Technology, Shanghai University, Shaoxing 312074, Zhejiang Province, China;
4. Shanghai Institute of Aircraft Mechanics and Control, Shanghai 200092, China

(Received Dec. 6, 2024 / Revised Feb. 11, 2025)

Abstract Designing, modeling, and analyzing novel nonlinear elastic elements for the nonlinear energy sink (NES) have long been an attractive research topic. Since gravity is difficult to overcome, previous NES research mainly focused on horizontal vibration suppression. This study proposes an origami-inspired NES. A stacked Miura-origami (SMO) structure, consisting of two Miura-ori sheets, is adopted to construct a nonlinear elastic element. By adjusting the initial angle and the connecting crease torsional stiffness, the quasi-zero stiffness (QZS) and load-bearing capacity can be customized to match the corresponding mass, establishing the vertical SMO-NES. The dynamic model of the SMO-NES coupled with a linear oscillator (LO) is derived for vibrations in the vertical direction. The approximate analytical solutions of the dynamic equation are obtained by the harmonic balance method (HBM), and the solutions are verified numerically. The parameter design principle of the SMO-NES is provided. Finally, the vibration reduction performance of the SMO-NES is studied. The results show that the proposed SMO-NES can overcome gravity and achieve quasi-zero nonlinear restoring force. Therefore, the SMO-NES has the ability of wide-frequency vibration reduction, and can effectively suppress vertical vibrations. By adjusting the initial angle and connecting the crease torsional stiffness of the SMO, the SMO-NES can be achieved with different loading weights, effectively suppressing the vibrations with different primary system masses and excitation amplitudes. In conclusion, with the help of popular origami structures, this study proposes a novel NES, and starts the research of combining origami and NES.

Key words nonlinear energy sink (NES), stacked Miura-origami (SMO), vertical vibration, quasi-zero stiffness (QZS)

* Citation: ZENG, Y. C., DING, H., and JI, J. C. An origami-inspired nonlinear energy sink: design, modeling, and analysis. *Applied Mathematics and Mechanics* (*English Edition*), **46**(4), 601–616 (2025) https://doi.org/10.1007/s10483-025-3239-6

† Corresponding author, E-mail: dinghu3@shu.edu.cn

Project supported by the National Science Fund for Distinguished Young Scholars (No. 12025204) and the China Scholarship Council (No. 202206890066)

Chinese Library Classification O322
2010 Mathematics Subject Classification 34A34, 74H45

1 Introduction

Controlling vertical-direction vibrations in structures has become increasingly critical[1–2]. Prolonged vertical vibrations can cause fatigue, crack formation, and structural failure in buildings and bridges, especially in earthquake-prone areas[3]. They can also loosen mechanical equipment components, accelerate wear, and lead to equipment failure. Excessive vertical vibrations in vehicles (such as trains and cars) and airplanes can affect passenger comfort and safety[4]. Therefore, effective vertical vibration control is urgently needed.

A tuned mass damper (TMD) is a passive device designed to reduce vibrations in structures[5]. Its frequency is tuned to match one of the natural frequencies of the target structure. However, if the excitation frequency changes, the effectiveness of the TMD would substantially decrease. Furthermore, when a structure exhibits multiple vibration modes, a single TMD can suppress only one mode, with limited influence on the others[6]. These two drawbacks severely constrain the engineering applications of TMDs.

The nonlinear energy sink (NES) is a passive nonlinear device[7–12]. Due to its unique nonlinear coupling and broadband absorption characteristics[13–16], the NES has significant advantages in suppressing complex broadband vibrations[17–23]. Compared with traditional TMDs, NESs can operate effectively over a wider frequency range and possess higher adaptability[24–27]. Wang et al.[28] proposed a bistable side-track NES with asymmetric structures, and experimentally demonstrated that the NES can effectively reduce horizontal vibrations. Zeng et al.[29] proposed a stable state adjustable NES to suppress the horizontal vibrations of different excitation intensities. Geng et al.[30] proposed a magnetically limited NES to improve the reliability of NESs, and showed that the limitation of nonlinear magnetic force enhanced the horizontal vibration suppression effect and reduced the vibrations of the NES. Kremer and Liu[31] used an NES consisting of a fixed beam and magnets to suppress horizontal vibrations and harvest energy. Al-Shudeifat et al.[32] and Saeed et al.[33] experimentally and numerically studied the use of the rotating NES in passive nonlinear target energy transfer, and found that the rotating NES could effectively suppress horizontal vibration. The above research proves that NESs have remarkable vibration reduction efficiency for horizontal vibrations. However, for the main system with dominant vertical vibrations in engineering practice, the equilibrium position is affected by the NES gravity. The initial deformation caused by the gravity of an NES will increase the linear stiffness of the NES[34–35], thereby weakening its wideband vibration reduction capability. Thus, designing novel NESs that can eliminate the unexpected effects of gravity in vertical motion will overcome the limitations of the existing NESs in attenuating vertical vibrations, and requires more research effort.

Origami structures can be formulated based on the art of paper folding, where folded and planar geometric shapes create forms with specific functions and structural characteristics[36]. Due to their unique geometric properties, adjustability, and lightweight, origami structures have found broad applications in engineering and science, emerging as an innovative method in engineering design[37]. Origami structures based on quasi-zero stiffness (QZS) characteristics are an innovative vibration isolation technology, which allows for low dynamic stiffness within small displacement ranges, effectively isolating low-frequency vibrations[38–39]. Ye and Ji[40–41] and Ye et al.[42] proposed a QZS isolator formed by stacking Miura-origami structures with truss springs, which could provide the required ultra-low dynamic stiffness for isolation while maintaining high static stiffness for load support capacity, achieving effective suppression of low-frequency vibrations. The origami structures based on the QZS characteristics have a certain load support capacity and low dynamic linear stiffness, fully meeting the design requirements for effectively suppressing the vertical vibration of an NES. However, to the best of the authors'

knowledge, there has been no research on origami-based NES design.

Inspired by the benefit of the origami structures, to suppress vertical vibrations, this study develops the structural design of origami-inspired NES for the first time. This study proposes a stacked Miura-origami (SMO)-NES model, and conducts the parameter design and vibration reduction analysis for the SMO-NES. The results indicate that the proposed SMO-NES can effectively suppress vertical vibrations. The main structure of the work is arranged as follows. The mechanical model and the derivation of the dynamic equations are presented in Section 2. Section 3 shows the parameter design principles of the SMO-NES. Section 4 performs a polynomial fitting analysis for the nonlinear restoring force, and introduces the approximate analytical solutions to the dynamic equations. Section 5 studies the vibration reduction of the SMO-NES. Finally, the conclusions are summarized.

2 Mechanical model

The SMO configuration (see Fig. 1(a)) consists of two standard Miura-ori sheets, i.e., Sheet A and Sheet B. First, both Miura-ori units are folded individually according to their crease patterns (dashed lines represent valley folds, and solid lines represent mountain folds). Then, the corresponding edges in the middle of the two folded units are connected to form the SMO.

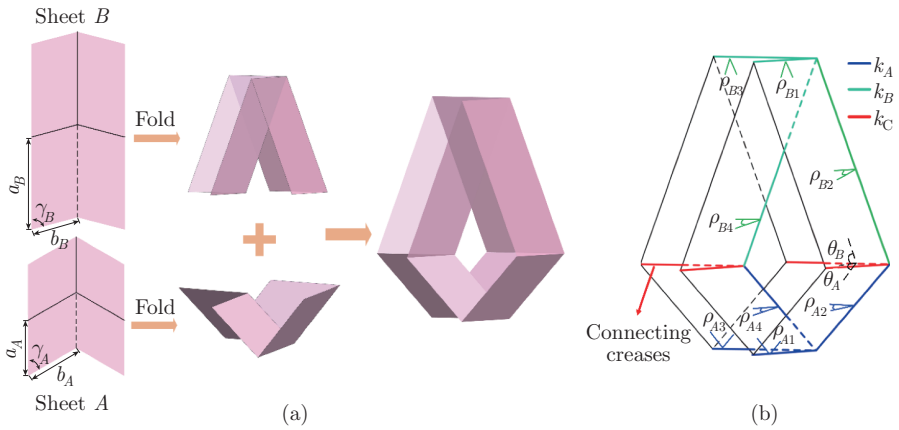

Fig. 1 Structure of the SMO: (a) configuration; (b) geometry (color online)

A standard Miura-ori unit can be defined by two adjacent crease lines, i.e., a_i and b_i, and the angle γ_i between them ($i = A, B$). To ensure planar rigidity and compatibility during the motion of the SMO structure, the geometric parameters must satisfy

$$\frac{\cos\gamma_B}{\cos\gamma_A} = \frac{a_A}{a_B}, \quad b_A = b_B = b, \quad \cos\theta_B \tan\gamma_B = \cos\theta_A \tan\gamma_A, \tag{1}$$

where θ_A and θ_B represent the fold angles of the two Miura-ori units concerning the horizontal plane along the connecting edge.

The folding motion of the SMO structure can be described by the dihedral angles between adjacent faces, and the relationship between these dihedral angles and the fold angles satisfies the following conditions:

$$\begin{cases} \rho_{i1} = \rho_{i3} = \pi - 2\theta_i, \quad \rho_{i2} = 2\arcsin\left(\dfrac{\cos\theta_i}{\sqrt{1-\sin^2\theta_i\sin^2\gamma_i}}\right), \\ \rho_{i4} = 2\pi - \rho_{i2}, \quad \rho_{\mathrm{C}} = \theta_B - \theta_A, \end{cases} \tag{2}$$

where ρ_{i1}, ρ_{i2}, ρ_{i3}, and ρ_{i4} are the dihedral angles, and ρ_{C} is the dihedral angle corresponding to the crease along the connecting edge.

The vertical height H can be expressed as follows:

$$H = a_B \sin\theta_B \sin\gamma_B - a_A \sin\theta_A \sin\gamma_A. \tag{3}$$

In the SMO configuration, the dihedral angles $\rho_{Aj}\,(j = 1, 2, 3, 4)$ correspond to the crease lines with a torsional stiffness K_{Aj}. The dihedral angles $\rho_{Bj}\,(j = 1, 2, 3, 4)$ correspond to the crease lines with a torsional stiffness K_{Bj}. The dihedral angle ρ_{C} is related to a crease line with a torsional stiffness K_{C}. Furthermore, $K_{A1} = K_{A3} = k_A b$, $K_{A2} = K_{A4} = k_A a_A$, $K_{B1} = K_{B3} = k_B b$, $K_{B2} = K_{B4} = k_B a_B$, and $K_{\mathrm{C}} = k_{\mathrm{C}} b$, where k_A and k_B are the torsional stiffnesses per unit length of the creases in Sheet A and Sheet B, respectively, and k_{C} is the connecting crease torsional stiffness per unit length.

The total potential energy U of the SMO structure can be written as follows:

$$U = \frac{1}{2}\Big(\sum_{j=1}^{4} K_{Aj}(\Delta\rho_{Aj})^2 + \sum_{j=1}^{4} K_{Bj}(\Delta\rho_{Bj})^2 + 4K_{\mathrm{C}}(\Delta\rho_{\mathrm{C}})^2\Big). \tag{4}$$

The initial height H_0 of the SMO structure can be expressed as follows:

$$H_0 = a_B \sin\theta_{B0} \sin\gamma_B - a_A \sin\theta_{A0} \sin\gamma_A, \tag{5}$$

where θ_{A0} and θ_{B0} represent the angles of θ_A and θ_B in the initial state, respectively.

Therefore, the vertical displacement y of the SMO structure is given by

$$y = H_0 - H. \tag{6}$$

By differentiating the potential energy U with respect to the vertical displacement y, the nonlinear restoring force of the SMO structure can be obtained as follows:

$$F(y) = \frac{\mathrm{d}U}{\mathrm{d}y} = \frac{\mathrm{d}U}{\mathrm{d}\theta_A} \cdot \Big(\frac{\mathrm{d}y}{\mathrm{d}\theta_A}\Big)^{-1}. \tag{7}$$

Figure 2 shows that the SMO-NES consists of a mass m_2 and an SMO structure that provides the nonlinear restoring force $F(y)$. The SMO-NES is then coupled with a linear oscillator (LO) in the vertical direction. m_1, c_1, and k_1 represent the mass, damping, and stiffness of the LO, respectively. A vertical force excitation $F_1 = F_0\cos(\omega t)$ is applied to the LO, where ω is the excitation frequency, and F_0 is the amplitude of the excitation force.

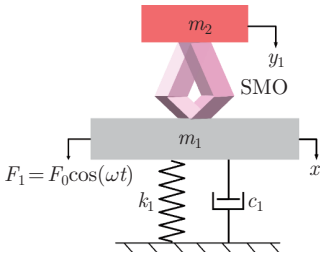

Fig. 2 Schematic diagram of the SMO-NES coupled LO (color online)

When the mass of the SMO-NES is m_2, assume that y_1 is the relative displacement between the static equilibrium position of the SMO-NES and the LO. Then, according to Newton's

second law, the dynamic equations of the coupled system are given by

$$\begin{cases} m_1\dfrac{\mathrm{d}^2x}{\mathrm{d}t^2}+c_1\dfrac{\mathrm{d}x}{\mathrm{d}t}+k_1x-F(y_1)-c_2\dfrac{\mathrm{d}y_1}{\mathrm{d}t}=F_0\cos(\omega t)+m_1g, \\ m_2\left(\dfrac{\mathrm{d}^2y_1}{\mathrm{d}t^2}+\dfrac{\mathrm{d}^2x}{\mathrm{d}t^2}\right)+c_2\dfrac{\mathrm{d}y_1}{\mathrm{d}t}+F(y_1)=m_2g. \end{cases} \tag{8}$$

3 Parameter design

In this section, to obtain the SMO structures with load support capacity and QZS characteristics, the effects of the initial angle θ_{A0} and the connecting crease torsional stiffness per unit length k_C on the nonlinear restoring force, nonlinear stiffness, and equilibrium bifurcation are studied. The geometric parameters of the SMO are listed in Table A1[44]. It should be noted that, for a more concise representation of the relationship between radians and degrees, the radian expressions in this study have not been simplified.

Figure 3 shows the variations of the nonlinear restoring force, nonlinear stiffness, and equilibrium bifurcation diagram with the initial angle θ_{A0} when $k_C = 0.863\,\mathrm{N/(rad\cdot m)}$. When θ_{A0} changes from $-70\pi/180$ to $-30\pi/180$, the stable state of the SMO-NES is transmitted from bistable to monostable. When $\theta_{A0} = -60\pi/180$, there is one pitchfork (PF) bifurcation of the equilibrium solution, and the PF bifurcation point satisfies the QZS condition. Figure 4 shows the variations of the nonlinear restoring force, nonlinear stiffness, and equilibrium bifurcation diagram with the connecting crease torsional stiffness per unit length k_C when $\theta_{A0} = -60\pi/180$. Similar to the influence of θ_{A0}, as k_C increases, the stable state of the SMO-NES changes from bistable to monostable. When $k_C = 0.863\,\mathrm{N/(rad\cdot m)}$, there is one PF bifurcation. It is noted that the value of the nonlinear restoring force corresponding to zero stiffness is defined as the loading weight G of the SMO-NES.

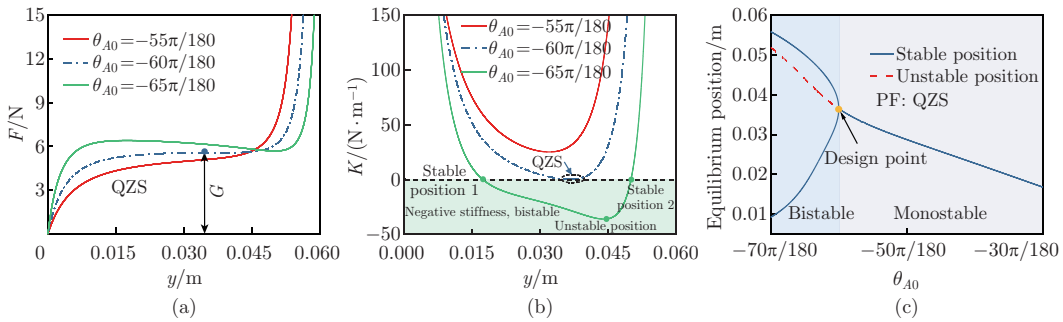

Fig. 3 Variations of (a) the nonlinear restoring force and (b) the nonlinear stiffness. (c) Equilibrium bifurcation diagram of the SMO-NES when $k_C = 0.863\,\mathrm{N/(rad\cdot m)}$ (color online)

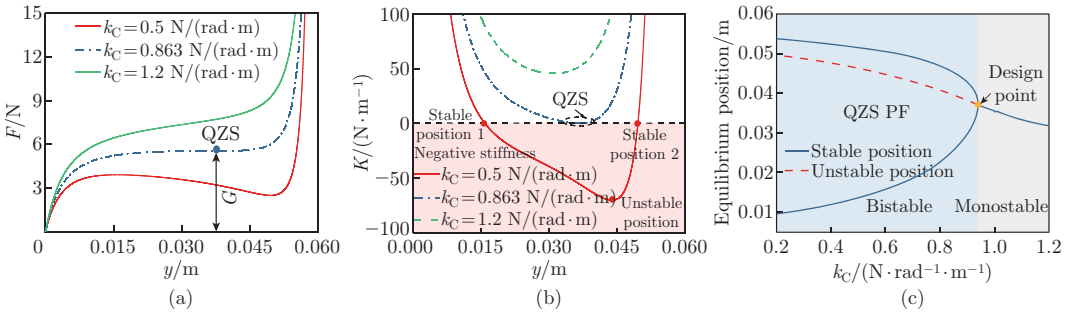

Fig. 4 Variations of (a) the nonlinear restoring force and (b) the nonlinear stiffness. (c) Equilibrium bifurcation diagram of the SMO-NES when $\theta_{A0} = -60\pi/180$ (color online)

As shown in Fig. 5, in order to achieve the SMO-NES with QZS characteristic, as θ_{A0} varies from $-70\pi/180$ to $-30\pi/180$, k_{C} gradually decreases, resulting in a corresponding reduction in the loading weight G of the SMO-NES. Therefore, for the primary systems with different masses, adjusting θ_{A0} and k_{C} allows for the tuning of the loading weight G of the SMO-NES, thereby achieving effective vibration suppression.

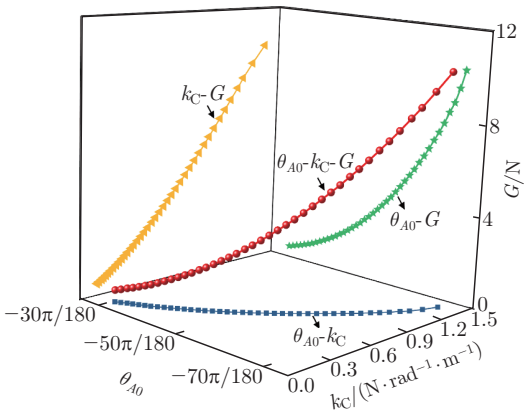

Fig. 5 The relationship of θ_{A0}, k_{C}, and G under the QZS condition (color online)

4 Approximate analytical solution

The coordinate transformation relationship is shown in Fig. 6. Assume that y_1 is the static equilibrium position (the position where the stiffness is zero) of the SMO-NES. At this point, the gravity of the SMO-NES mass m_2 equals the loading weight G, i.e., $G = m_2 g$. For a vertical vibration system, the static equilibrium positions x_{s} and y_{s} of the main system and the SMO-NES under the action of gravity are defined by the following algebraic equations:

$$k_1 x_{\mathrm{s}} - F(y_{\mathrm{s}}) = m_1 g, \quad F(y_{\mathrm{s}}) = G. \tag{9}$$

The expressions for x_{s} and y_{s} are obtained as

$$x_{\mathrm{s}} = (m_1 g + G)/k_1, \quad y_{\mathrm{s}} = 0. \tag{10}$$

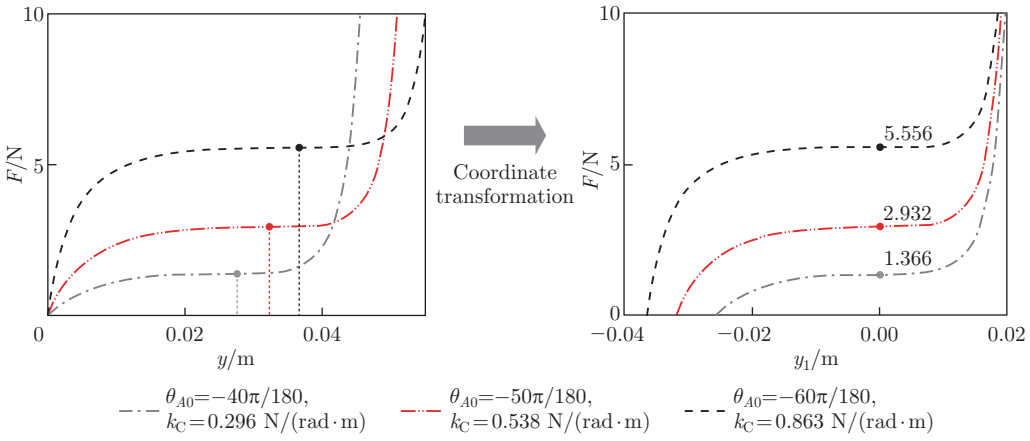

Fig. 6 Coordinate transformation relationship (color online)

Introduce the relative displacements measured from the static equilibrium, i.e., $x_1 = x - x_s$ and $Y_1 = y_1 - y_s$. Then, the dynamic equations of the coupled system about the gravitational equilibrium are obtained as

$$\begin{cases} m_1 \dfrac{\mathrm{d}^2 x_1}{\mathrm{d}t^2} + c_1 \dfrac{\mathrm{d}x_1}{\mathrm{d}t} + k_1 x_1 + G - F(y_1) - c_2 \dfrac{\mathrm{d}y_1}{\mathrm{d}t} = F_0 \cos(\omega t), \\ m_2 \left(\dfrac{\mathrm{d}^2 y_1}{\mathrm{d}t^2} + \dfrac{\mathrm{d}^2 x_1}{\mathrm{d}t^2} \right) + c_2 \dfrac{\mathrm{d}y_1}{\mathrm{d}t} + F(y_1) - G = 0. \end{cases} \tag{11}$$

4.1 Polynomial fitting

To obtain the approximate analytical solutions for the coupled system, the polynomial fitting is applied to the nonlinear restoring force of the SMO-NES. Figure 7 presents the results of the polynomial fitting, showing that as the order of the polynomial increases, the fitting accuracy improves. Furthermore, it can be observed that the nonlinear restoring force of the SMO-NES is distinctly asymmetric.

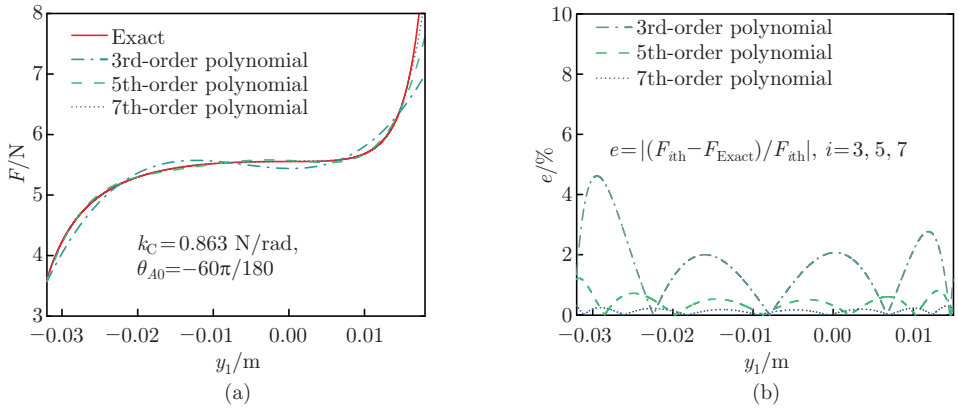

Fig. 7 Polynomial fitting results: (a) nonlinear restoring force; (b) error ratio (color online)

To balance computational time and accuracy, a 7th-order polynomial fitting is selected in this study. Thus, the nonlinear restoring force of the SMO-NES can be expressed as

$$F(y_1) = G + B_1 y_1 + B_2 y_1^2 + B_3 y_1^3 + B_4 y_1^4 + B_5 y_1^5 + B_6 y_1^6 + B_7 y_1^7. \tag{12}$$

Table A2 presents the polynomial coefficients for the nonlinear restoring force of the SMO-NES when $\theta_{A0} = -60\pi/180$ and $k_C = 0.863\,\mathrm{N/(rad \cdot m)}$.

4.2 Harmonic balance method (HBM)

To obtain the approximate analytical solutions of the coupled system, the HBM is used in this study. Therefore, the solution to Eq. (11) can be assumed as

$$\begin{cases} x_1(t) = c_{1,0} + \displaystyle\sum_{n=1}^{N} \cos(n\omega t) a_{1,n} + \sum_{n=1}^{N} \sin(n\omega t) b_{1,n}, \\ y_1(t) = c_{2,0} + \displaystyle\sum_{n=1}^{N} \cos(n\omega t) a_{2,n} + \sum_{n=1}^{N} \sin(n\omega t) b_{2,n}, \end{cases} \tag{13}$$

where $a_{1,n}$, $b_{1,n}$, $a_{2,n}$, and $b_{2,n}$ are the undetermined coefficients for the corresponding harmonic terms, and n is the harmonic order. In view of the significant asymmetry observed in the nonlinear restoring force of the SMO-NES, the constant terms $c_{1,0}$ and $c_{2,0}$ must be taken

into account. N is the maximum harmonic order. By using the pseudo-arc-length extension process, the singularity can be easily avoided, allowing the solution of the algebraic equations to be obtained. By substituting the harmonic coefficients calculated from this process into Eq. (13), the response of the coupled system can be obtained. Furthermore, the stability of the computed solutions is determined by the Floquet stability theory[43].

5 Vibration reduction analysis

The vibration reduction efficiency of the SMO-NES is defined first. Then, the parameters and schematic diagrams of five different initial angles θ_{A0} corresponding to the connecting crease torsional stiffness per unit length k_{C} and loading weight G are given. Finally, the dynamics and vibration reduction efficiency of the SMO-NES under five different initial angles θ_{A0} are studied in detail.

The vibration reduction efficiency ξ is defined as follows:

$$\xi = \frac{|\max(A_{\mathrm{W}}) - \max(A_{\mathrm{WO}})|}{\max(A_{\mathrm{WO}})} \times 100\%, \tag{14}$$

where A_{W} and A_{WO} are the amplitude-frequency responses of the LO coupled and uncoupled with the SMO-NES, respectively. Since the unstable solutions of the HBM cannot reliably predict the unstable solutions, the vibration reduction efficiency is calculated through numerical methods. Furthermore, to assure the accuracy of the calculation results, the maximum harmonic order of the HBM is $N = 3$, and the numerical solutions are obtained through the fourth-order Runge-Kutta (RK) method.

Table 1 lists the crease torsional stiffness per unit length k_{C} and loading weight G when $\theta_{A0} = -30\pi/180$, $-40\pi/180$, $-50\pi/180$, $-60\pi/180$, and $-70\pi/180$. It can be seen that when θ_{A0} decreases from $-30\pi/180$ to $-70\pi/180$, k_{C} gradually increases, and G also gradually increases.

Table 1 Five different initial angles θ_{A0} and the corresponding crease torsional stiffness k_{C} and loading weight G

θ_{A0}	$-30\pi/180$	$-40\pi/180$	$-50\pi/180$	$-60\pi/180$	$-70\pi/180$
$k_{\mathrm{C}}/(\mathrm{N}\cdot\mathrm{rad}^{-1}\cdot\mathrm{m}^{-1})$	0.122	0.296	0.538	0.863	1.378
G/N	0.515	1.366	2.932	5.556	10.21
Schematic diagram					

The parameters of the LO are $m_1 = 20\,\mathrm{kg}$, $k_1 = 14\,870\,\mathrm{N}\cdot\mathrm{m}^{-1}$, and $c_1 = 1.8\,\mathrm{N}\cdot\mathrm{s}\cdot\mathrm{m}^{-1}$. The damping of the SMO-NES is $c_2 = 0.9\,\mathrm{N}\cdot\mathrm{s}\cdot\mathrm{m}^{-1}$. The excitation amplitude is $F_0 = 2\,\mathrm{N}$. The nonlinear stiffness and mass of the SMO-NES are determined from Table A1. Figure 8 shows the amplitude-frequency responses of the LO and the vibration reduction efficiency of the SMO-NES for different θ_{A0}, k_{C}, and G. Figure 9 shows the displacement of the LO, the displacement of the SMO-NES, and the spectrum of the SMO-NES for different θ_{A0}, k_{C}, and G. First, it can be observed that the numerical solutions and approximate analytical solutions are in good agreement with each other, indicating the correctness of the calculation results obtained in this study. When $\theta_{A0} = -30\pi/180$, $k_{\mathrm{C}} = 0.122\,\mathrm{N}/(\mathrm{rad}\cdot\mathrm{m})$, $G = 0.514\,5\,\mathrm{N}$, and $\varepsilon = m_2/m_1 = 0.262\,5\%$, the vibration reduction efficiency is the worst. The displacement responses of the LO and SMO-NES are periodic. Due to the asymmetry of the nonlinear restoring force of the SMO-NES, there is a significant zero drift phenomenon in the frequency spectrum of

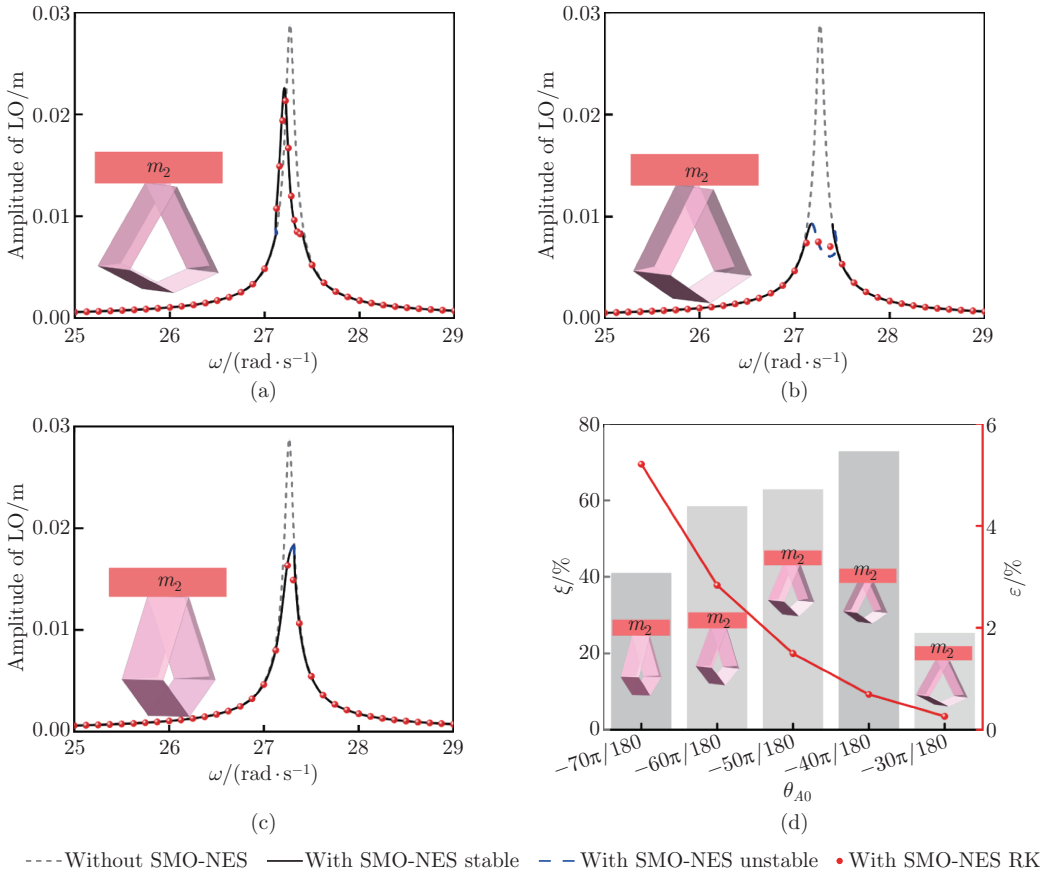

Fig. 8 The amplitude-frequency responses of the LO under different parameters: (a) $\theta_{A0} = -30\pi/180$, $k_C = 0.122\,\mathrm{N/(rad\cdot m)}$, $F_0 = 2\,\mathrm{N}$, $m_1 = 20\,\mathrm{kg}$, $G = 0.514\,5\,\mathrm{N}$, and $\varepsilon = 0.262\,5\%$; (b) $\theta_{A0} = -40\pi/180$, $k_C = 0.296\,\mathrm{N/(rad\cdot m)}$, $F_0 = 2\,\mathrm{N}$, $m_1 = 20\,\mathrm{kg}$, $G = 1.366\,\mathrm{N}$, and $\varepsilon = 0.696\,9\%$; (c) $\theta_{A0} = -70\pi/180$, $k_C = 1.387\,\mathrm{N/(rad\cdot m)}$, $F_0 = 2\,\mathrm{N}$, $m_1 = 20\,\mathrm{kg}$, $G = 10.21\,\mathrm{N}$, and $\varepsilon = 5.209\,2\%$. (d) Vibration reduction efficiency with different initial angles θ_{A0} when $m_1 = 20$ and $F_0 = 2\,\mathrm{N}$(color online)

the SMO-NES, and there also exist some harmonic components. When $\theta_{A0} = -40\pi/180$, $k_C = 0.296\ \mathrm{N/(rad\cdot m)}$, $G = 1.366\,\mathrm{N}$, and $\varepsilon = 0.696\,9\%$, as the mass ratio increases, the vibration reduction efficiency is significantly improved. From the amplitude-frequency response of the LO, it can be observed that there is a wide range of unstable frequencies in the resonance region. The displacement responses of both the LO and SMO-NES exhibit significant strong modulation responses. When $\theta_{A0} = -70\pi/180$, $k_C = 1.387\ \mathrm{N/(rad\cdot m)}$, $G = 10.21\,\mathrm{N}$, and $\varepsilon = 5.209\,2\%$, it can be seen from the amplitude-frequency response of the LO that the unstable region in the resonance zone narrows, and the vibration reduction efficiency decreases. The displacement responses of both the LO and SMO-NES also show that the strong modulation response weakens. As θ_{A0} changes from $-30\pi/180$ to $-70\pi/180$, the loading weight G of the SMO-NES gradually increases, the mass ratio ε increases accordingly, and the vibration reduction efficiency first increases and then decreases. The highest vibration reduction efficiency occurs when $\theta_{A0} = -40\pi/180$ and $\varepsilon = 0.696\,9\%$.

The mass of the LO, m_1, is changed to investigate the wideband vibration reduction performance of the SMO-NES. The LO mass is set to $m_1 = 10\,\mathrm{kg}$ and $m_1 = 30\,\mathrm{kg}$, with the initial angle θ_{A0} varying from $-70\pi/180$ to $-30\pi/180$. The excitation amplitude is $F_0 = 2\,\mathrm{N}$.

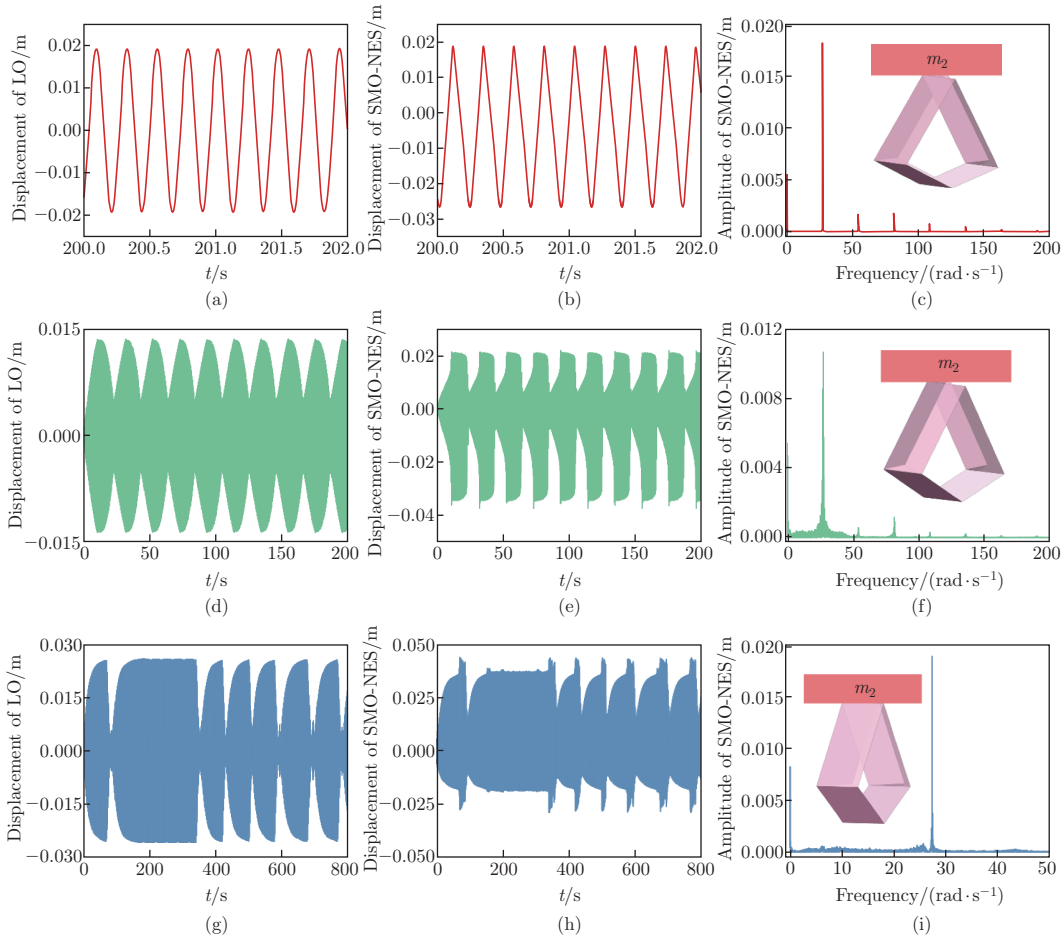

Fig. 9 Displacement of the LO (left), displacement of the SMO-NES (middle), and spectrum of the SMO-NES (right) for (a)–(c) $\theta_{A0} = -30\pi/180$, $k_C = 0.122\,\mathrm{N/(rad \cdot m)}$, $G = 0.514\,5\,\mathrm{N}$; (d)–(f) $\theta_{A0} = -40\pi/180$, $k_C = 0.296\,\mathrm{N/(rad \cdot m)}$, $G = 1.366\,\mathrm{N}$, $F_0 = 2\,\mathrm{N}$, and $\omega = 27.27\,\mathrm{rad/s}$; (g)–(i) $\theta_{A0} = -70\pi/180$, $k_C = 1.387\,\mathrm{N/(rad \cdot m)}$, $G = 10.21\,\mathrm{N}$, $F_0 = 2\,\mathrm{N}$, and $\omega = 27.31\,\mathrm{rad/s}$ (color online)

Figure 10 shows that when $m_1 = 10\,\mathrm{kg}$, the highest vibration reduction efficiency is achieved at $\theta_{A0} = -30\pi/180$, where the loading weight of the SMO-NES is $G = 0.515\,\mathrm{N}$, and the mass ratio ε is 0.525%. When $m_1 = 30\,\mathrm{kg}$, the highest vibration reduction efficiency occurs when $\theta_{A0} = -50\pi/180$, with the loading weight of the SMO-NES G of $2.932\,\mathrm{N}$ and the mass ratio of 0.997%. From Figs. 9 and 10, it can be observed that adjusting the initial angle and the connecting crease torsional stiffness allows for obtaining the SMO-NES with different loading weights, enabling effective vibration control for primary systems of varying masses. Additionally, the larger the mass of the LO, the greater the loading weight required for the corresponding initial angle and connecting crease torsional stiffness.

Next, the influence of the excitation amplitude on the dynamics and vibration reduction efficiency of the SMO-NES is investigated. The parameters of the LO are $m_1 = 20\,\mathrm{kg}$, $k_1 = 14\,870\,\mathrm{N \cdot m^{-1}}$, and $c_1 = 1.8\,\mathrm{N \cdot s \cdot m^{-1}}$. The damping of the SMO-NES is $c_2 = 0.9\,\mathrm{N \cdot s \cdot m^{-1}}$. The excitation amplitude is changed to $F_0 = 2.5\,\mathrm{N}$. Figure 11 shows the amplitude-frequency responses of the LO and the vibration reduction efficiency of the SMO-NES with different θ_{A0}, k_C, and G. Figure 12 shows the displacement of LO, the displacement of SMO-NES,

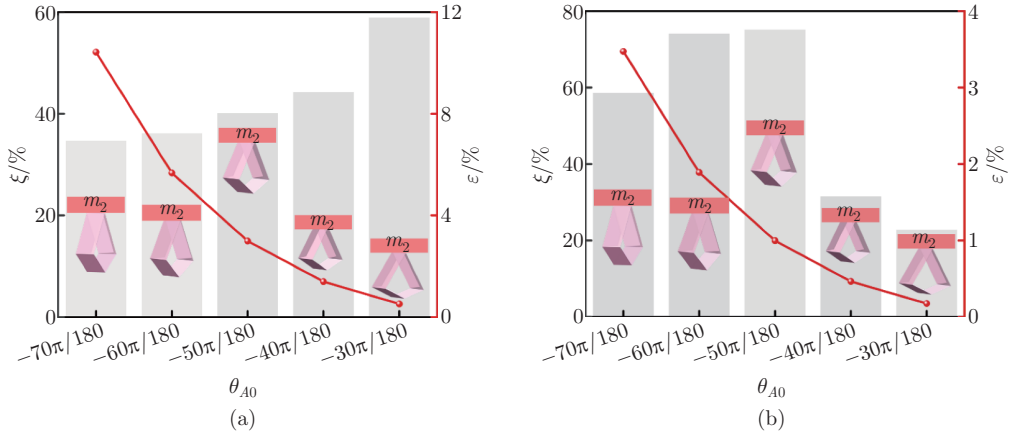

Fig. 10 Mass ratio and vibration reduction efficiency of the SMO-NES when (a) $m_1 = 10\,\text{kg}$ and $F_0 = 2\,\text{N}$; (b) $m_1 = 30\,\text{kg}$ and $F_0 = 2\,\text{N}$ (color online)

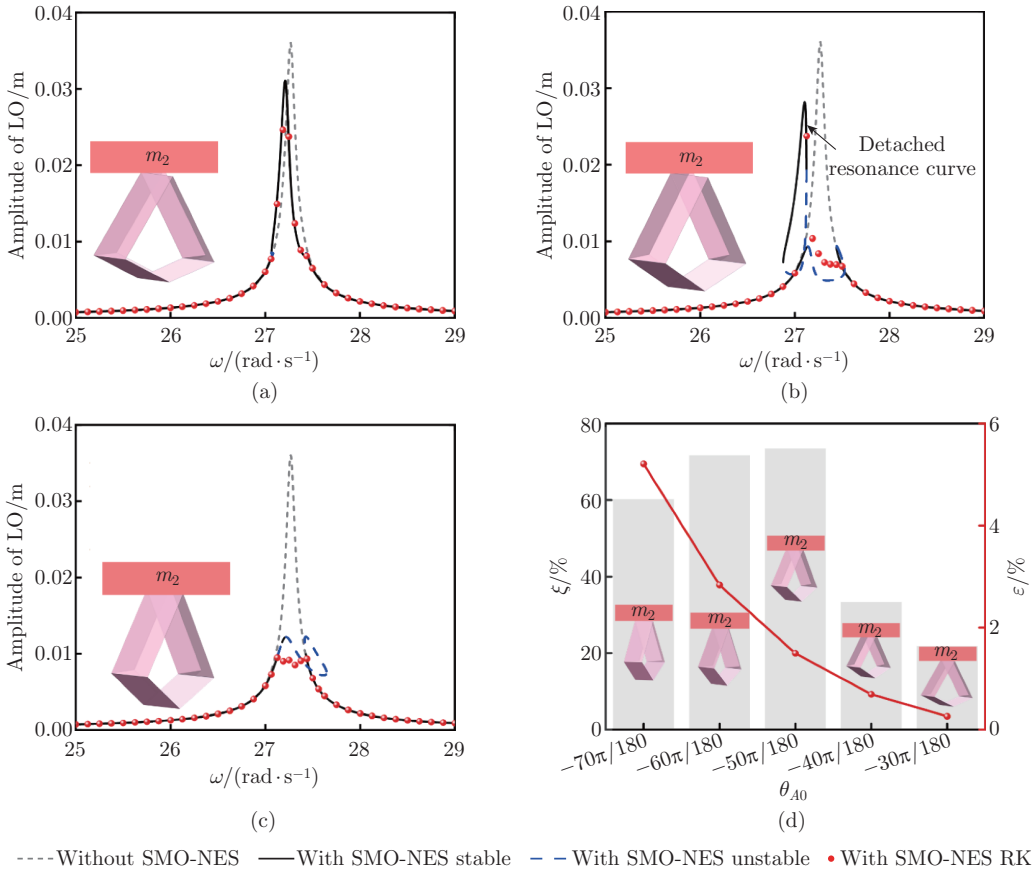

Fig. 11 Amplitude-frequency responses when (a) $\theta_{A0} = -30\pi/180$, $k_C = 0.122\,\text{N/(rad}\cdot\text{m)}$, $F_0 = 2.5\,\text{N}$, $m_1 = 20\,\text{kg}$, $G = 0.5145\,\text{N}$, and $\varepsilon = 0.2625\%$; (b) $\theta_{A0} = -40\pi/180$, $k_C = 0.296\,\text{N/(rad}\cdot\text{m)}$, $F_0 = 2.5\,\text{N}$, $m_1 = 20\,\text{kg}$, $G = 1.366\,\text{N}$, and $\varepsilon = 0.6969\%$; (c) $\theta_{A0} = -50\pi/180$, $k_C = 0.538\,\text{N/(rad}\cdot\text{m)}$, $F_0 = 2.5\,\text{N}$, $m_1 = 20\,\text{kg}$, $G = 2.932\,\text{N}$, and $\varepsilon = 1.4959\%$. (d) Vibration reduction efficiency and mass ratio with different initial angle θ_{A0} when $m_1 = 20\,\text{kg}$ and $F_0 = 2.5\,\text{N}$ (color online)

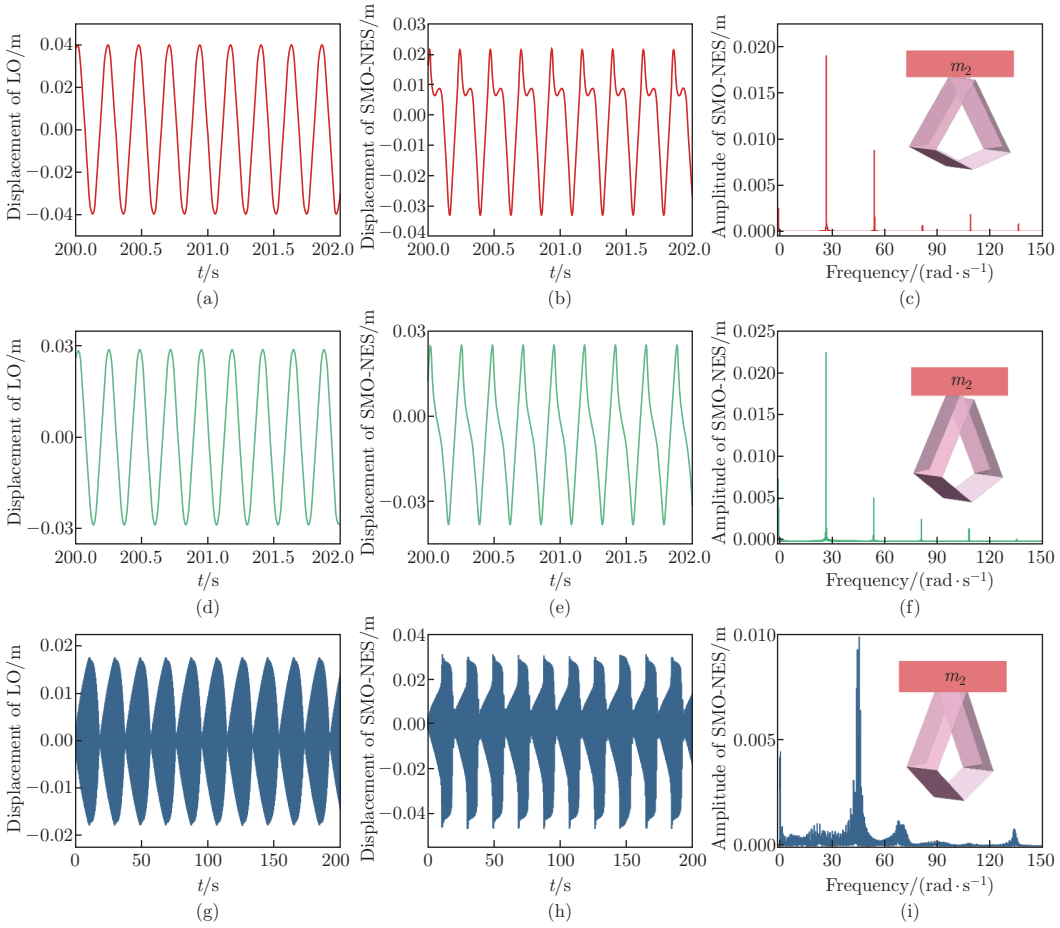

Fig. 12 Displacement of the LO (left), displacement of the SMO-NES (middle), and spectrum of the SMO-NES (right) for (a)–(c) $\theta_{A0} = -30\pi/180$, $k_{\mathrm{C}} = 0.122\,\mathrm{N/(rad \cdot m)}$, $G = 0.514\,5\,\mathrm{N}$, $F_0 = 2.5\,\mathrm{N}$, and $\omega = 27.22\,\mathrm{rad/s}$; (d)–(f) $\theta_{A0} = -40\pi/180$, $k_{\mathrm{C}} = 0.296\,\mathrm{N/(rad \cdot m)}$, $G = 1.366\,\mathrm{N}$, $F_0 = 2.5\,\mathrm{N}$, and $\omega = 27.06\,\mathrm{rad/s}$; (g)–(i) $\theta_{A0} = -50\pi/180$, $k_{\mathrm{C}} = 0.538\,\mathrm{N/(rad \cdot m)}$, $G = 2.932\,\mathrm{N}$, $F_0 = 2.5\,\mathrm{N}$, and $\omega = 27.27\,\mathrm{rad/s}$ (color online)

and the spectrum of the SMO-NES with different θ_{A0}, k_{C}, and G. When $\theta_{A0} = -30\pi/180$, $k_{\mathrm{C}} = 0.122\,\mathrm{N/(rad \cdot m)}$, $G = 0.514\,5\,\mathrm{N}$, and $\varepsilon = 0.262\,5\%$, the vibration reduction efficiency is the worst. The displacement responses of the LO and SMO-NES are periodic. When $\theta_{A0} = -40\pi/180$, $k_{\mathrm{C}} = 0.296\,\mathrm{N/(rad \cdot m)}$, $G = 1.366\,\mathrm{N}$, and $\varepsilon = 0.696\,9\%$, a detached resonance curve appears in the amplitude-frequency response of the LO, which shows no improvement in the vibration reduction efficiency of the SMO-NES. When $\theta_{A0} = -50\pi/180$, $k_{\mathrm{C}} = 0.538\,\mathrm{N/(rad \cdot m)}$, $G = 2.932\,\mathrm{N}$, and $\varepsilon = 1.495\,9\%$, as the mass ratio ε continues to increase, the vibration reduction efficiency is significantly improved. From the amplitude-frequency response of the LO, it can be observed that there is a wide range of unstable frequencies in the resonance region. The displacement responses of both the LO and SMO-NES exhibit significant strong modulation responses. As the initial angle changes from $-70\pi/180$ to $-30\pi/180$, the loading weight of the SMO-NES gradually decreases, and the mass ratio decreases accordingly. The vibration reduction efficiency first increases, and then decreases. The highest vibration reduction efficiency occurs when $\theta_{A0} = -50\pi/180$, where the mass ratio ε is $1.495\,9\%$.

Similarly, by varying the excitation amplitude, the vibration reduction efficiency of the SMO-

NES is investigated under different θ_{A0} and k_C. Figure 13(a) shows that when the excitation amplitude $F_0 = 4.5\,\mathrm{N}$, the highest vibration reduction efficiency is achieved at the initial angle θ_{A0} of $-60\pi/180$, where $G = 5.556\,\mathrm{N}$ and $\varepsilon = 1.304\%$. As depicted in Fig. 13(b), when the excitation amplitude increases to $F_0 = 7\,\mathrm{N}$, the highest vibration reduction efficiency occurs at the initial angle θ_{A0} of $-70\pi/180$, the SMO-NES loading weight reaches 10.21 N, and the mass ratio is 5.209%. Combining the observations from Figs. 11 and 13, it is evident that by adjusting the initial angle and connecting crease torsional stiffness per unit length, the SMO-NES units with different load support capacities can be obtained, thereby effectively suppressing the vibrations of varying excitation intensities. Furthermore, the greater the excitation amplitude, the larger the required loading weight of the SMO-NES.

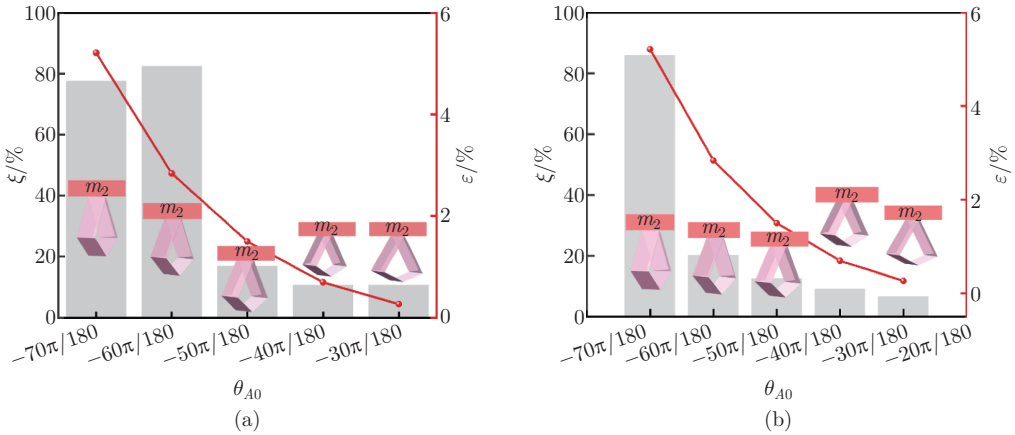

Fig. 13 Mass ratio and vibration reduction efficiency of the SMO-NES with different θ_{A0} and fixed F_0: (a) $F_0 = 4.5\,\mathrm{N}$, (b) $F_0 = 7\,\mathrm{N}$ (color online)

6 Conclusions

In this study, an SMO-NES is proposed, for the first time, to effectively suppress vertical vibrations. The SMO structure consists of two standard Miura-ori sheets. The dynamic equations of the coupled system are derived in the vertical direction. The approximate analytical solutions are obtained, and the solutions are verified numerically. The main findings are summarized as follows.

(i) By adjusting the initial angle and the connecting crease torsional stiffness of the SMO structure, the QZS and load-bearing capacity can be customized to match the corresponding mass.

(ii) The proposed SMO-NES has the ability of wide-frequency vibration reduction, and can effectively suppress vertical vibrations.

(iii) The larger the mass of the primary system, the greater the loading weight of the SMO-NES required. The greater the excitation amplitude, the greater the required loading weight of the SMO-NES.

In short, the proposed SMO-NES in this study provides a new solution for improving the broadband vibration reduction performance of traditional NESs in vertical systems. In the future, origami configuration and NES design will be further combined, and the advantages of the SMO-NES will be explored through theory, experiment, and application.

Conflict of interest Hu DING is an editorial board member for *Applied Mathematics and Mechanics* (*English Edition*) and was not involved in the editorial review or the decision to publish this

article. The authors declare no conflict of interest.

References

[1] CHILLEMI, M., FURTMÜLLER, T., ADAM, C., and PIRROTTA, A. Fluid inerter-based vibration control of multi-modal structures subjected to vertical vibration. *Engineering Structures*, **307**, 117938 (2024)

[2] LIU, C. C., JING, X. J., DALEY, S., and LI, F. M. Recent advances in micro-vibration isolation. *Mechanical Systems and Signal Processing*, **56-57**, 55–80 (2015)

[3] GUZMAN PUJOLS, J. C. and RYAN, K. L. Computational simulation of slab vibration and horizontal-vertical coupling in a full-scale test bed subjected to 3D shaking at E-Defense. *Earthquake Engineering & Structural Dynamics*, **47**(2), 438–459 (2017)

[4] TOWARD, M. G. R. and GRIFFIN, M. J. The transmission of vertical vibration through seats: influence of the characteristics of the human body. *Journal of Sound and Vibration*, **330**(26), 6526–6543 (2011)

[5] ZHU, Y. N., GUO, X. Y., WANG, Q., and CAO, D. X. A lightweight tuned particle damper for low-frequency vibration attenuation. *Journal of Sound and Vibration*, **583**, 118440 (2024)

[6] ABÉ, M. and FUJINO, Y. Dynamic characterization of multiple tuned mass dampers and some design formulas. *Earthquake Engineering & Structural Dynamics*, **23**(8), 813–835 (2007)

[7] ZHANG, Y. F., KONG, X. R., YUE, C. F., and GUO, J. S. Characteristic analysis and design of nonlinear energy sink with cubic damping considering frequency detuning. *Nonlinear Dynamics*, **111**(17), 15817–15836 (2023)

[8] VAKAKIS, A. F., MANEVITCH, L. I., GENDELMAN, O., and BERGMAN, L. Dynamics of linear discrete systems connected to local, essentially non-linear attachments. *Journal of Sound and Vibration*, **264**(3), 559–577 (2003)

[9] LI, M., LI, S. B., and DING, H. Analysis of damping efficiency of nonlinear energy sink cell (in Chinese). *Chinese Journal of Theoretical and Applied Mechanics*, **55**(11), 2614–2623 (2023)

[10] CAO, Y. B., YAO, H. L., HAN, J. C., LI, Z. A., and WEN, B. C. Application of non-smooth NES in vibration suppression of rotor-blade systems. *Applied Mathematical Modelling*, **87**, 351–371 (2020)

[11] GAO, Q. Y. and YANG, T. Z. A nonlinear vibration isolator with an essentially nonlinear converter. *Applied Mathematical Modelling*, **136**, 115648 (2024)

[12] LI, W. K., WANG, Z. M., BRENNAN, M. J., and YANG, T. J. Design and optimization of a two-degrees-of-freedom single-sided vibro-impact nonlinear energy sink for transient vibration suppression of a thin plate. *Journal of Sound and Vibration*, **587**, 118512 (2024)

[13] LIAO, X., CHEN, L., ZHOU, S., and ZHANG, M. L. A novel vari-potential bistable nonlinear energy sink for improved vibration suppression: numerical and experimental study. *Nonlinear Dynamics*, **111**(21), 19763–19790 (2023)

[14] DOU, J. X., YAO, H. L., LI, H., LI, J. L., and JIA, R. Y. A track nonlinear energy sink with restricted motion for rotor systems. *International Journal of Mechanical Sciences*, **259**, 108631 (2023)

[15] LI, S. B., ZHOU, X. X., and CHEN, J. E. Hamiltonian dynamics and targeted energy transfer of a grounded bistable nonlinear energy sink. *Communications in Nonlinear Science and Numerical Simulation*, **117**, 106898 (2023)

[16] MA, K., DU, J. T., LIU, Y., and CHEN, X. M. Torsional vibration attenuation of a closed-loop engine crankshaft system via the tuned mass damper and nonlinear energy sink under multiple operating conditions. *Mechanical Systems and Signal Processing*, **207**, 110941 (2024)

[17] DING, H. and CHEN, L. Q. Designs, analysis, and applications of nonlinear energy sinks. *Nonlinear Dynamics*, **100**(4), 3061–3107 (2020)

[18] WANG, J. J. and ZHENG, Y. Q. Development and robustness investigation of track-based asymmetric nonlinear energy sink for impulsive response mitigation. *Engineering Structures*, **286**, 116127 (2023)

[19] WANG, Y., WANG, P. L., MENG, H. D., and CHEN, L. Q. Dynamic performance and parameter optimization of a half-vehicle system coupled with an inerter-based X-structure nonlinear energy sink. *Applied Mathematics and Mechanics* (*English Edition*), **45**(1), 85–110 (2023) http://doi.org/10.1007/s10483-024-3070-7

[20] WANG, Y., ZHANG, T., YIN, Y., and WEI, X. H. Reducing shimmy oscillation of a dual-wheel nose landing gear based on torsional nonlinear energy sink. *Nonlinear Dynamics*, **112**(6), 4027–4062 (2024)

[21] DOU, J. X., YAO, H. L., CAO, Y. B., HAN, S. D., and BAI, R. X. Enhancement of bistable nonlinear energy sink based on particle damper. *Journal of Sound and Vibration*, **547**, 117547 (2023)

[22] YAO, H. L., CAO, Y. B., ZHANG, S. J., and WEN, B. C. A novel energy sink with piecewise linear stiffness. *Nonlinear Dynamics*, **94**(3), 2265–2275 (2018)

[23] ZHANG, S. T., ZHOU, J. X., DING, H., and WANG, K. Micro-vibration mitigation of a cantilever beam by one-third power nonlinear energy sinks. *Aerospace Science and Technology*, **153**, 109409 (2024)

[24] DING, H. and SHAO, Y. F. NES cell. *Applied Mathematics and Mechanics* (*English Edition*), **43**(12), 1793–1804 (2022) https://doi.org/10.1007/s10483-022-2934-6

[25] RONCEN, T., MICHON, G., and MANET, V. Design and experimental analysis of a pneumatic nonlinear energy sink. *Mechanical Systems and Signal Processing*, **190**, 110088 (2023)

[26] AL-SHUDEIFAT, M. A. Highly efficient nonlinear energy sink. *Nonlinear Dynamics*, **76**(4), 1905–1920 (2014)

[27] CHEN, J. E., SUN, M., HU, W. H., ZHANG, J. H., and WEI, Z. C. Performance of non-smooth nonlinear energy sink with descending stiffness. *Nonlinear Dynamics*, **100**(1), 255–267 (2020)

[28] WANG, J. J., ZHENG, Y. Q., MA, Y. H., and WANG, B. Experimental study on asymmetric and bistable nonlinear energy sinks enabled by side tracks. *Mechanical Systems and Signal Processing*, **206**, 110874 (2024)

[29] ZENG, Y. C., DING, H., JI, J. C., and CHEN, L. Q. Theoretical and experimental study of a stable state adjustable nonlinear energy sink. *Mechanical Systems and Signal Processing*, **216**, 111470 (2024)

[30] GENG, X. F., DING, H., JING, X. J., MAO, X. Y., WEI, K. X., and CHEN, L. Q. Dynamic design of a magnetic-enhanced nonlinear energy sink. *Mechanical Systems and Signal Processing*, **185**, 109813 (2023)

[31] KREMER, D. and LIU, K. F. A nonlinear energy sink with an energy harvester: harmonically forced responses. *Journal of Sound and Vibration*, **410**, 287–302 (2017)

[32] AL-SHUDEIFAT, M. A., WIERSCHEM, N. E., BERGMAN, L. A., and VAKAKIS, A. F. Numerical and experimental investigations of a rotating nonlinear energy sink. *Meccanica*, **52**(4-5), 763–779 (2016)

[33] SAEED, A. S., NASAR, R. A., and AL-SHUDEIFAT, M. A. A review on nonlinear energy sinks: designs, analysis and applications of impact and rotary types. *Nonlinear Dynamics*, **111**(1), 1–37 (2022)

[34] CHEN, L. Q., LI, X., LU, Z. Q., ZHANG, Y. W., and DING, H. Dynamic effects of weights on vibration reduction by a nonlinear energy sink moving vertically. *Journal of Sound and Vibration*, **451**, 99–119 (2019)

[35] LI, X., DING, H., and CHEN, L. Q. Effects of weights on vibration suppression via a nonlinear energy sink under vertical stochastic excitations. *Mechanical Systems and Signal Processing*, **173**, 109073 (2022)

[36] LIU, S. W., PENG, G. L., and JIN, K. Towards accurate modeling of the Tachi-Miura origami in vibration isolation platform with geometric nonlinear stiffness and damping. *Applied Mathematical Modelling*, **103**, 674–695 (2022)

[37] FANG, H. B., CHANG, T. S., and WANG, K. W. Magneto-origami structures: engineering multi-stability and dynamics via magnetic-elastic coupling. *Smart Materials and Structures*, **29**(1), 015026 (2020)

[38] JI, J. C., LUO, Q. T., and YE, K. Vibration control based metamaterials and origami structures: a state-of-the-art review. *Mechanical Systems and Signal Processing*, **161**, 107945 (2021)

[39] YU, K. F., CHEN, Y. W., YU, C. Y., LI, P., REN, Z. H., ZHANG, J. R., and LU, X. Origami-inspire quasi-zero stiffness structure for flexible low-frequency vibration isolation. *International Journal of Mechanical Sciences*, **276**, 109377 (2024)

[40] YE, K. and JI, J. C. An origami inspired quasi-zero stiffness vibration isolator using a novel truss-spring based stack Miura-ori structure. *Mechanical Systems and Signal Processing*, **165**, 108383 (2022)

[41] YE, K. and JI, J. C. Dynamic analysis of the effects of self-weight induced structural and damping nonlinearity on the performance of an origami-inspired vibration isolator. *Journal of Sound and Vibration*, **547**, 117538 (2023)

[42] YE, K., JI, J. C., and FITCH, R. Further investigation and experimental study of an origami structure-based quasi-zero-stiffness vibration isolator. *International Journal of Non-Linear Mechanics*, **157**, 104554 (2023)

[43] ZANG, J., YUAN, T. C., LU, Z. Q., ZHANG, Y. W., DING, H., and CHEN, L. Q. A lever-type nonlinear energy sink. *Journal of Sound and Vibration*, **437**, 119–134 (2018)

[44] SUN, X. T., LV, Q., QIAN, J. W., and XU, J. Vibration isolation platform for large-amplitude-low-frequency excitation by parallel-stack-assembly design of Miura origamis. *International Journal of Non-Linear Mechanics*, **166**, 104831 (2024)

Appendix A

Table A1 Geometric parameters of the SMO[44]

Parameter	Value	Unit
a_A	38	mm
a_B	73.4	mm
b	38	mm
γ_A	$\pi/3$	rad
γ_B	$5\pi/12$	rad
k_A	0.03	$\mathrm{N\cdot rad^{-1}\cdot m^{-1}}$
k_B	1	$\mathrm{N\cdot rad^{-1}\cdot m^{-1}}$
k_{C}	0.865	$\mathrm{N\cdot rad^{-1}\cdot m^{-1}}$

Table A2 Results of the polynomial fitting for the nonlinear restoring force coefficients

Symbol	Value	Unit
G	5.556	N
B_1	3.727	$\mathrm{N\cdot m^{-1}}$
B_2	-61.650	$\mathrm{N\cdot m^{-2}}$
B_3	3.392×10^{4}	$\mathrm{N\cdot m^{-3}}$
B_4	1.218×10^{6}	$\mathrm{N\cdot m^{-4}}$
B_5	6.599×10^{8}	$\mathrm{N\cdot m^{-5}}$
B_6	3.370×10^{10}	$\mathrm{N\cdot m^{-6}}$
B_7	5.297×10^{11}	$\mathrm{N\cdot m^{-7}}$